Intrinsic torque reversals induced by magnetic shear effects on the turbulence spectrum in tokamak plasmasa)

Z. X. Lu, W. X. Wang, P. H. Diamond, G. Tynan, S. Ethier, C. Gao, and J. Rice

Citation: Physics of Plasmas (1994-present) **22**, 055705 (2015); doi: 10.1063/1.4919395
View online: http://dx.doi.org/10.1063/1.4919395
View Table of Contents: http://scitation.aip.org/content/aip/journal/pop/22/5?ver=pdfcov
Published by the AIP Publishing

Intrinsic torque reversals induced by magnetic shear effects on the turbulence spectrum in tokamak plasmas[a)]

Z. X. Lu,[1,2,b)] W. X. Wang,[3] P. H. Diamond,[2] G. Tynan,[1,2] S. Ethier,[3] C. Gao,[4] and J. Rice[4]
[1]*Center for Energy Research and Department of Mechanical and Aerospace Engineering, University of California at San Diego, San Diego, California 92093, USA*
[2]*Center for Momentum Transport and Flow Organization and Center for Astrophysics and Space Science, University of California, San Diego, California 92093, USA*
[3]*Princeton Plasma Physics Laboratory, Princeton, New Jersey 08540, USA*
[4]*Plasma Science and Fusion Center, Massachusetts Institute of Technology, Cambridge, Massachusetts 02139, USA*

(Received 14 November 2014; accepted 16 February 2015; published online 4 May 2015)

Intrinsic torque, which can be generated by turbulent stresses, can induce toroidal rotation in a tokamak plasma at rest without direct momentum injection. Reversals in intrinsic torque have been inferred from the observation of toroidal velocity changes in recent lower hybrid current drive (LHCD) experiments. This work focuses on understanding the cause of LHCD-induced intrinsic torque reversal using gyrokinetic simulations and theoretical analyses. A new mechanism for the intrinsic torque reversal linked to magnetic shear ($\hat{s}$) effects on the turbulence spectrum is identified. This reversal is a consequence of the ballooning structure at weak $\hat{s}$. Based on realistic profiles from the Alcator C-Mod LHCD experiments, simulations demonstrate that the intrinsic torque reverses for weak $\hat{s}$ discharges and that the value of $\hat{s}_{crit}$ is consistent with the experimental results $\hat{s}_{crit}^{exp} \approx 0.2 \sim 0.3$ [Rice *et al.*, Phys. Rev. Lett. **111**, 125003 (2013)]. The consideration of this intrinsic torque feature in our work is important for the understanding of rotation profile generation at weak $\hat{s}$ and its consequent impact on macro-instability stabilization and micro-turbulence reduction, which is crucial for ITER. It is also relevant to internal transport barrier formation at negative or weakly positive $\hat{s}$. © *2015 AIP Publishing LLC*. [http://dx.doi.org/10.1063/1.4919395]

I. BACKGROUND AND MOTIVATION

Intrinsic or spontaneous flows have been widely studied in many contexts since they are ubiquitous in physics. They are a key factor in understanding various phenomena such as solar differential rotation,[1] formation of the tachocline,[2] and atmospheric jet stream.[3] Intrinsic torque, which can be generated by turbulent stresses, is associated with the self-organization of flow patterns.[4] In the presence of eddies or wave turbulence, intrinsic flow is related to the classic turbulent magnetic dynamo problem.[5] In tokamak plasmas, toroidal rotation can develop due to intrinsic torque density τ_I, i.e., the divergence of residual stress $\Pi_{r\phi}^R$, without direct external momentum injection.[6,7] Generally, the Reynolds stress, whose divergence gives the related momentum transport, can be decomposed into diffusive, pinch, and residual parts.[8] Unlike the momentum diffusion and momentum pinch, which depend on the equilibrium toroidal velocity (V_ϕ) or its radial derivative (dV_ϕ/dr), the residual stress relies on the underlying turbulence properties rather than V_ϕ or dV_ϕ/dr and thus can accelerate the tokamak plasma from rest. One evidence of the existence of the intrinsic torque is the "cancellation" experiment on DIIID, where the rotation-free plasma is obtained through the cancellation between the intrinsic torque and the external torque applied by neutral beams.[9] Intrinsic rotation can mitigate macroscopic instability[10] and regulate microscopic instability, thus reducing turbulent transport. In addition, intrinsic rotation is particularly important for the International Thermonuclear Experimental Reactor (ITER), since neutral beam injection (NBI) is not sufficient to drive the requisite rotation on large tokamaks.

Rotation reversal experiments present a compelling challenge to our understanding of intrinsic torque, especially of its direction. Toroidal rotation reversal during Ohmic phase has been observed, particularly in response to the change in electron density.[11,12] In rotation experiments with lower hybrid current drive (LHCD), changes in V_ϕ (toroidal velocity) during LHCD with both co- and counter-current directions have been observed in different devices.[13,14] In recent studies of rotation in experiments with LHCD on Alcator C-Mod, ΔV_ϕ reversed from high LH power (P_{LH}) discharges to low P_{LH} discharges, where ΔV_ϕ is the change in the core rotation velocity in toroidal direction from pre-LHCD phase to the end of LHCD.[15] For these discharges, high P_{LH} corresponds to high plasma current I_p, low q in the whole radial range, normal (or relatively high) $\hat{s}$ in the core ($r/a < 0.5$), and counter-current directed ΔV_ϕ, and vice versa for low P_{LH}. In addition, for high I_p discharges, the toroidal velocity in the core changes direction. This observation suggests that these profiles are not the results of a momentum pinch or momentum diffusion, which would only change the profile shape but not reverse the direction. Motivated by experimental evidence[6,15] and theoretical understanding,[8] it is hypothesized that the observed reversal

[a)]Paper NI2 4, Bull. Am. Phys. Soc. **59**, 195 (2014).
[b)]Invited speaker.

of ΔV_ϕ is due to the reversal in the underlying intrinsic torque. In the plasma core, the intrinsic torque during LHCD is in the counter-current direction when $\hat{s}$ is normal and reverses when $\hat{s}$ is lower than a critical value $\hat{s}_{crit}$. In these discharges, $\hat{s}$ is above zero in the whole radial range, increases monotonically with r, and rotation changes mainly for $r/a < 0.5$. Experimental results show that torque reversal occurs for $\hat{s} < \hat{s}^{exp}_{crit} \approx 0.2 \sim 0.3$, where $\hat{s}^{exp}_{crit}$ is estimated at $r/a \sim 0.3$. To understand the experimental results, the effects of $\hat{s}$ on the intrinsic torque reversal need to be studied. Since both q and $\hat{s}$ change among different discharges in the LHCD rotation reversal experiments, a critical value of on-axis safety factor q_0 for ΔV_ϕ reversal has also been observed, corresponding to the critical magnetic shear $\hat{s}_{crit}$. As a result, the effect of q should also be clarified.

Understanding the effect of the q-profile structure on the intrinsic torque is also an issue of interest in the context of internal transport barrier (ITB) formation and profile "destiffening," which occur not only in negative magnetic shear but also in regimes of weak but non-negative magnetic shear.[16] ITB formation is believed to be related to the microturbulence suppression and the consequent transport reduction by $\mathbf{E} \times \mathbf{B}$ shear flows and thus is related to the toroidal rotation via the radial force balance equation, i.e., $E_r = (1/en_i)dp_i/dr - V_\theta B_\phi + V_\phi B_\theta$, where E_r is radial electric field, p_i is ion pressure, n_i is ion density, V_θ and V_ϕ are poloidal and toroidal velocities, and B_θ, B_ϕ are magnetic fields in poloidal and toroidal directions.[17] While NBI is the main toroidal momentum source in some ITB experiments,[18,19] the contribution of intrinsic torque can be important for toroidal rotation profile formation, particularly in balanced-injection cases (with negligible net NBI momentum),[20] and for large-size devices such as ITER or DEMO where the NBI is not a sufficient momentum source. As a result, it is important to understand the effect of $\hat{s}$ on intrinsic torque, which is closely linked to how the toroidal rotation profile evolves for weakly positive or reversed $\hat{s}$, and affects the $\mathbf{E} \times \mathbf{B}$ shear flows and thus ITB generation.

This work focuses on understanding the cause of the LHCD-induced intrinsic torque reversal related to the q profile structure. Based on our simulations and analyses, a new symmetry breaking mechanism in residual stress generation is identified, which becomes dominant at weak $\hat{s}$ and leads to the intrinsic torque reversal. Intrinsic torque τ_I reversal for weak magnetic shear $\hat{s}$ is found in our simulations compared to normal $\hat{s}$; τ_I reverses when $\hat{s} < 0.3$ for collisionless trapped electron mode (CTEM) and when $\hat{s} < 1.3$ for ion temperature gradient (ITG) mode. Negative $\hat{s}$ is not required for the intrinsic torque reversal. Analyses show that this mechanism is due to the effect of weak shear on the ballooning structure modes and its impact on the spectral intensity gradient induced residual stress. At weak $\hat{s}$, the synergy of toroidal coupling and the intensity gradient effects induces significant radial eigenfunction shift and inverts the sign of spectrum averaged parallel wave vector $\langle k_{||} \rangle$ and thus the sign of the parallel residual stress. The critical value of $\hat{s}_{crit}$ is set by the competition between magnetic drift and ion finite Larmor radius (FLR) effects. Most of previous work on residual stress is for normal $\hat{s}$ regimes,[21,22] so the mechanism proposed in this letter has no antecedent. Based on realistic parameters of C-Mod LHCD experiments, simulation results show that the intrinsic torque changes from counter- to co-current direction as the core $\hat{s}$ change from normal to weak and ITG changes to CTEM, which is consistent with the experimental observation. The critical value of $\hat{s}$ for reversal as calculated by our simulations, i.e., $\hat{s}_{crit} \approx 0.3$, is also consistent with that indicated by experiments.

The remainder of this paper is organized as follows. In Sec. I, we introduce the GTS code, the parameter setup, and the basic simulation results, in particular, the intrinsic torque reversal when the magnetic shear $\hat{s}$ is lower than a critical, positive value. In Sec. II, the correlation and sensitivity studies are performed to identify the dominance of the intensity gradient symmetry breaking mechanism and the effect of $\hat{s}$ on intrinsic torque reversal. In Sec. III, the mode structure is analyzed based on the simulation results and eigenvalue approach to identify the new symmetry breaking for the intrinsic torque reversal related to weak $\hat{s}$, i.e., the radial eigenfunction shift due to the synergy of toroidal coupling and intensity gradient effects. In Sec. IV, we discuss the relevance to Alcator C-Mod LHCD experimental results and draw conclusions.

II. INTRINSIC TORQUE REVERSAL FOR WEAK AND NEGATIVE $\hat{s}$ COMPARED TO THAT FOR NORMAL $\hat{s}$

The gyrokinetic, particle-in-cell, δf code GTS[23,24] is used in our study. GTS is capable of capturing the key physics, e.g., global effects, in weak $\hat{s}$ regime, which are particularly relevant to this work. Typical tokamak parameters are adopted in our simulation study.[25] Equilibria with different q profiles are generated using the ESC code,[26] with pressure profile fixed. The equilibria are characterized by on-axis magnetic field value $B_{axis} \approx 2.55$ and outer boundary elongation $E = 1.45$ and triangularity $\kappa = 0.144$. Two types of q profiles are adopted, as shown in Fig. 1. The on-axis q_{min} profile has monotonic $q(r)$ and positive $\hat{s}$ in the whole radial range, while the off-axis q_{min} profile has q_{min} at r_{min} and negative $\hat{s}$ for $r < r_{min}$. The values of q and $\hat{s}$ at the reference radius r_c are chosen as $q(r_c) \sim 1$–2, $\hat{s} < 0.6$ in the following parametric studies, which is relevant to the rotation reversal experiments.[15] Profiles of temperature and density gradient are given by $R_0/L_{n,Ti,Te} = \kappa_{ne,Ti,Te} \exp\{-[(r - r_c)/0.2]^2\}$. The temperature and density profiles are calculated according to their gradient profiles and the reference values at r_c,

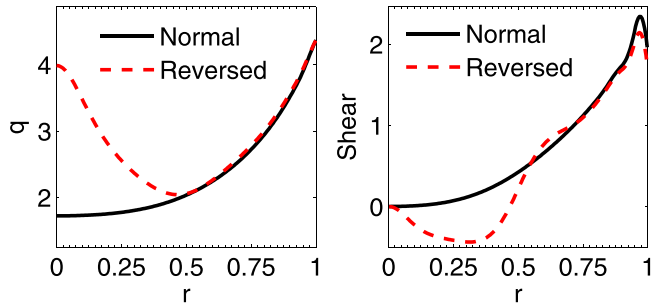

FIG. 1. Safety factor q and magnetic shear $\hat{s}$ profiles of two model equilibria, denoted as normal (black line) and reversed (red broken line).

$T_i = T_e = 3.5\,\mathrm{keV}$ and $n_i = n_e = 1.6 \times 10^{13}/\mathrm{cm}^3$. The turbulence is destabilized by the temperature and density gradient and propagates/spreads towards the inner and outer boundaries where a damping region is set as the sink. The magnetic shear at the drive location r_c has different values for different cases. The turbulence develops around r_c, where $\hat{s}|_{r_c}$ has a specific value; thus the effects of $\hat{s}$ on $\Pi^R_{r\phi}$ can be studied. Here $a/\rho_i \approx 160$, where a is the minor radius and ρ_i is the gyro-radius. Collisions between electrons and ions are simplified by neglecting the mass of electron, and thus the Lorentz operator is adopted to describe electron-ion collisions. The like-species collision operator is implemented by keeping the test particle drag and diffusion terms.[27] The equilibrium radial electric field E_{r0} is obtained from the radial force balance equation consistent with the toroidal rotation profile,[28] and the $E \times B$ flow effects are included by taking into account E_{r0} in the particle's equation of motion. Collisions and equilibrium $\mathbf{E} \times \mathbf{B}$ flow are included in the simulations for self-consistency. We set the background toroidal velocity to be zero to focus on the study of residual stress, since the momentum pinch and diffusion are less relevant to intrinsic torque reversal as mentioned in Sec. I. For nonlinear cases, the simulations are performed until the turbulence reaches a well saturated state, during which the toroidal momentum flux is calculated. Since the simulation is carried out on the turbulence time scale, which is much shorter than the transport time scale, as adopted by most of global gyro-kinetic PIC simulations, the background toroidal velocity change is negligible and the calculated toroidal momentum flux is thus due to residual stress. In addition, the relaxation of the temperature and density profiles is subdominant to the background drive, and thus the turbulence is maintained at a relatively steady level during the simulation time scale.

We first examine the intrinsic torque driven by turbulence for negative $\hat{s}$ and compare to that for normal $\hat{s}$. Since the divergence of residual stress gives the intrinsic torque, i.e., $\tau_I = -\nabla \cdot \Pi^R_{r\phi}$, the orientation change of the $\Pi^R_{r\phi}$ radial profile indicates the intrinsic torque reversal. In this work, we calculate residual stress to infer the direction of the intrinsic torque. Here, "normal $\hat{s}$" refers to the base case with on-axis q_{min} profile and $\hat{s}(r_c) \approx 0.6$ at the drive location r_c, while "negative $\hat{s}$" refers to the case with an off-axis q_{min} profile and $\hat{s}(r_c) \approx -0.3$. To isolate the dependence of the residual stress on the mode type, we choose $\kappa_{Ti} = 0$ to eliminate ITG instability and focus on CTEM turbulence. We choose $\eta_e \equiv \kappa_{Te}/\kappa_{ne} = 2$, $\kappa_{ne} = 2.25$ for normal shear and $\kappa_{ne} = 3$ for negative shear to compensate the stabilizing effect of the negative $\hat{s}$. The ITG case is discussed later. The spatio-temporal structure of the residual stress is shown in Fig. 2. Compared with the normal $\hat{s}$ case (Fig. 2(a)), for the negative $\hat{s}$ case, the orientation of the residual stress changes and thus the intrinsic torque reverses, as shown in Fig. 2(b). By comparing the radial structure of $\Pi^R_{r\phi}$ in the linear and nonlinear stage, we found that the radial profile of $\Pi^R_{r\phi}$ maintains a similar structure, as shown in Figs. 2(c) and 2(d). As a result, parametric scans, which are computationally intensive, can be performed based on the simulation in linear stage. A parametric scan is performed in negative $\hat{s}$ region by varying r_c and thus with $\hat{s}(r_c)$ ranging from -0.4 to 0. The intrinsic torque reversal is found if $\hat{s}(r_c) < 0$, which indicates that negative $\hat{s}$ is a sufficient condition for the intrinsic torque reversal in our accessible $\hat{s}$ regime.

One key question is whether a negative $\hat{s}$ is also necessary for the intrinsic torque reversal or whether a weak non-negative $\hat{s}$ is sufficient. To determine the condition for the intrinsic torque reversal, we examine the radial structure of $\Pi^R_{r\phi}$ at weak $\hat{s}$ and identify the critical magnetic shear value $\hat{s}_{crit}$ at which the intrinsic torque reverses. An equilibrium with a flat q, on-axis q_{min} profile is chosen with $\hat{s}(r_c) \approx 0.1$. The other parameters are the same as those in the previous negative magnetic shear case. As shown in Fig. 3(a), the residual stress has the opposite orientation compared to that of

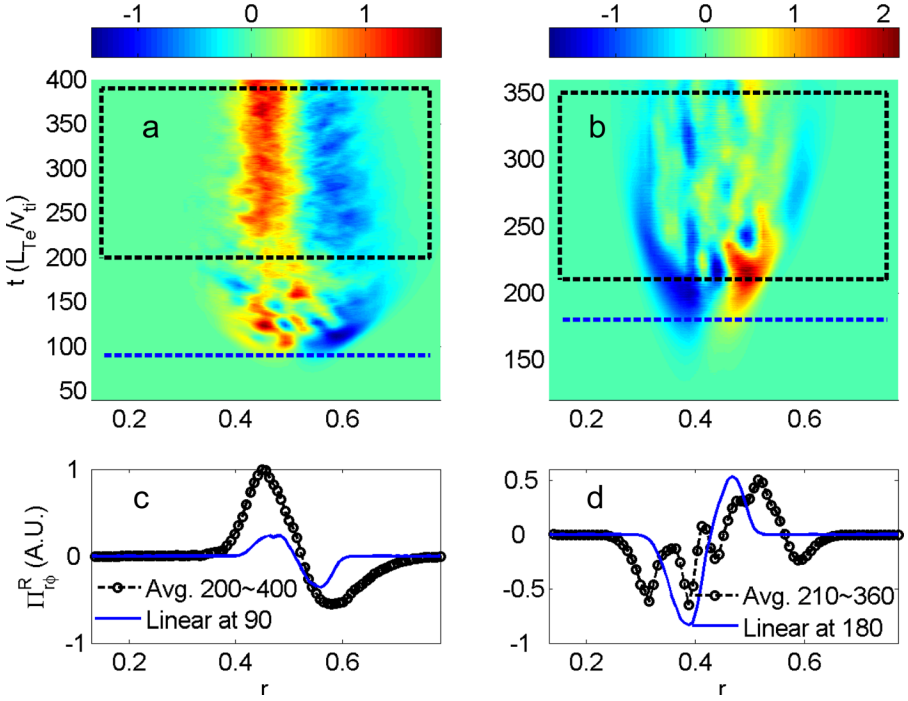

FIG. 2. Spatio-temporal structure of residual stress of normal (a) and negative (b) magnetic shear with $\hat{s}(r_c) \sim 0.6, -0.3$, respectively; comparison of residual stress during nonlinear stage and linear stage of normal (c) and negative (d) magnetic shear.

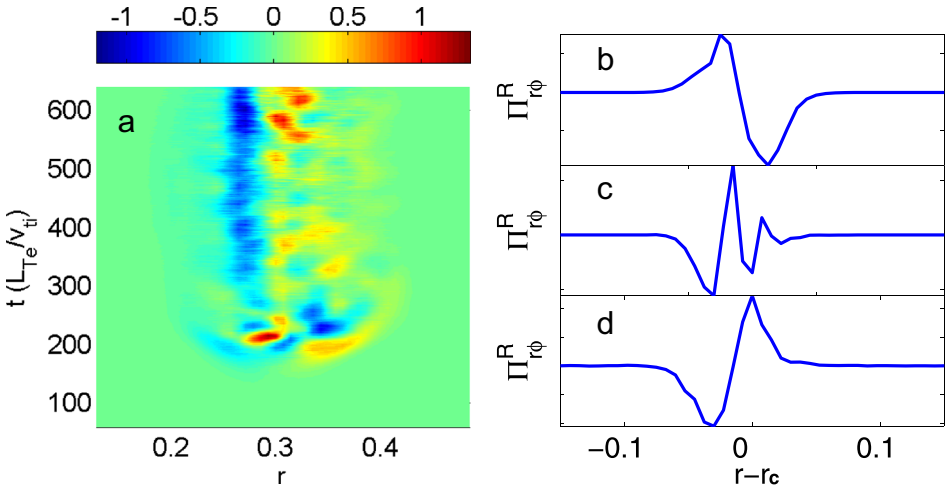

FIG. 3. (a) Spatio-temporal structure of residual stress for weak magnetic shear (flat q, on-axis q_{min}) profile with $\hat{s}(r_c) \sim 0.1$; radial structure of residual stress with (b) $\hat{s}(r_c) \sim 0.41$, (c) 0.32, and (d) 0.25, where r_c is the drive location.

the base case in Fig. 2(a). In order to find the critical magnetic shear at which the radial profile of $\Pi^R_{r\phi}$ changes orientation, a parametric scan of $\hat{s}(r_c)$ is performed. The orientation of residual stress is found to reverse when $\hat{s}(r_c)$ changes from 0.41 to 0.25, as shown in Figs. 3(b) and 3(d). Figure 3(c) demonstrates that the transition of residual stress occurs at $\hat{s} \approx 0.32$. This gives the critical value $\hat{s}_{crit}$ at which the CTEM-driven intrinsic torque reverses. This result shows that the intrinsic torque can reverse if $\hat{s}$ is lower than a critical, positive value. Surprisingly, magnetic shear reversal is thus not required for the intrinsic torque reversal. This observation helps to understand the torque reversal in Alcator C-Mod LHCD experiment for weak $\hat{s}$.[15]

In addition to CTEM turbulence, ITG turbulence is also studied. We choose $\kappa_{Te} = 0$, $\kappa_{Ti} = 4.5$ and $\eta_i \equiv \kappa_{Ti}/\kappa_{ni} = 3$ for the parametric scan using GTS. As shown in Fig. 4, the transition of the residual stress profile orientation occurs at $\hat{s} \approx 1.3$ (Fig. 4(b)), and thus the critical magnetic shear for the ITG-driven intrinsic torque reversal is found to be $\hat{s}^{ITG}_{crit} \approx 1.3$. It should be noted that if $\hat{s}(r_c)$ increases further ($\hat{s}(r_c) > 1.86$) or decreases further ($\hat{s}(r_c) < 0.95$), the dipole structure of residual stress is better maintained compared to that in Figs. 4(a) and 4(c). The direction of the intrinsic

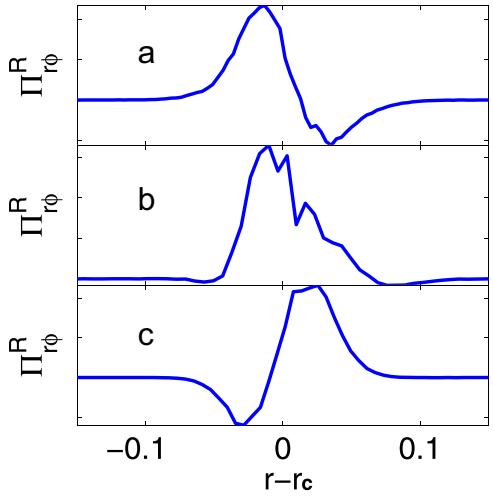

FIG. 4. Radial structure of residual stress $\Pi^R_{r\phi}$ with (a) $\hat{s}(r_c) \sim 1.86$, (b) 1.32, and (c) 0.95, where r_c is the drive location.

TABLE I. Summary of the torque direction of ITG/CTEM at the small minor radius side of the intensity peak. $\hat{s}^{CTEM}_{crit} \approx 0.3$, $\hat{s}^{ITG}_{crit} \approx 1.3$.

	$\hat{s} > \hat{s}^{ITG}_R$	$\hat{s}^{CTEM}_{crit} < \hat{s} < \hat{s}^{ITG}_{crit}$	$\hat{s} < \hat{s}^{CTEM}_{crit}$
CTEM	I. counter	II. *counter*	III. co
ITG	IV. counter	V. *co*	VI. co

torque, based on the divergence of residual stress at the small minor radius side of the intensity peak, is summarized in Table I. It is shown that the intrinsic torque has opposite directions for weak and high $\hat{s}$, both for ITG and CTEM turbulence. In addition, an intermediate shear region exists, where the intrinsic torque for ITG and CTEM turbulence has opposite directions. As a result, it is important to know both the magnetic shear regime and the mode type in predicting the direction of the intrinsic torque. The intrinsic torque reversal can occur when $\hat{s}$ regime and/or mode type change. For example, when $\hat{s}$ changes from normal to weak and CTEM changes to ITG (from regime II to VI), the intrinsic torque reverses, which is relevant to the Alcator C-Mod LHCD experiments as to be shown in Sec. IV. In realistic tokamak plasma, both ITG and CTEM turbulence can coexist in mixed state,[29] and the population of different modes and their contribution to the intrinsic torque should be properly estimated. The question of the intrinsic torque in mixed states merits more attention.

III. CORRELATION AND SENSITIVITY STUDIES OF THE INTRINSIC TORQUE REVERSAL

This section focuses on understanding the origin of the residual stress and its orientation change at weak $\hat{s}$, based on correlation and sensitivity studies. First, the correlation between residual stress and other variables is analyzed. The toroidal residual stress consists of parallel, perpendicular, and polarization toroidal stress, underpinned by correlators $\langle k_\parallel k_\theta |\delta\phi|^2\rangle$, $\langle k_r k_\theta |\delta\phi|^2\rangle$, and $\langle k_\parallel k_r |\delta\phi|^2\rangle$, where $\langle \ldots \rangle$ means spectrum average. The first and third correlators are connected to parallel symmetry breaking, while the second one is the toroidal projection of the total perpendicular stress. The total perpendicular stress contributes mainly to poloidal

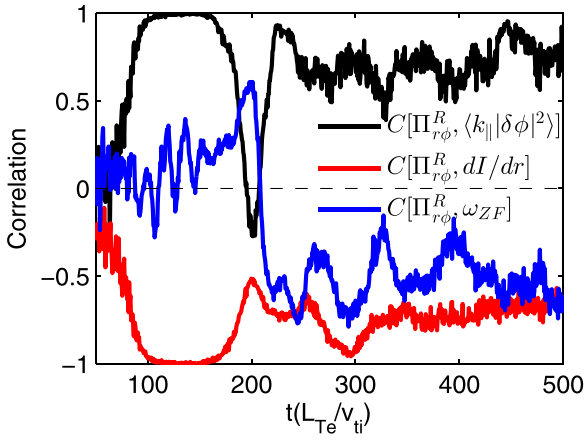

FIG. 5. Correlation between residual stress $\Pi^R_{r\phi}$ and spectrum weighted parallel wave vector $\langle k_\parallel|\delta\phi|^2\rangle$ (black line), correlation between $\Pi^R_{r\phi}$ and turbulence intensity gradient dI/dr (red line), and correlation between $\Pi^R_{r\phi}$ and zonal flow shear ω_{ZF} (blue line).

rotation. The $k_\parallel$ reversal can lead to $\Pi^R_{r\phi}$ reversal via the parallel and the polarization residual stress. As shown in Fig. 5, strong correlation among the turbulence intensity gradient dI/dr, the spectrum weighted parallel wave vector $\langle k_\parallel|\delta\phi|^2\rangle$ and the residual stress $\Pi^R_{r\phi}$ is observed. The average correlation coefficients during the nonlinear stage ($250 < t \times v_{ti}/L_{Te} < 500$) are $C[\Pi^R_{r\phi}, \langle k_\parallel|\delta\phi|^2\rangle] \approx 0.71$ and $C[\Pi^R_{r\phi}, dI/dr] \approx -0.74$, respectively, both of which have high magnitude (the sign of correlation indicates the phase relation). This supports the theory that the intensity gradient yields a finite $\langle k_\parallel|\delta\phi|^2\rangle$ and thus residual stress. However, it is found that $C[\Pi^R_{r\phi}, dI/dr]$ has the opposite sign compared to the normal $\hat{s}$ case, which indicates that the residual stress generation mechanism at weak $\hat{s}$ is different than the previous proposed one.[21] On the other hand, as zonal flow develops, which can largely affect turbulence transport at saturation,[30] zonal flow shear may also contribute to $\Pi^R_{r\phi}$ generation in the nonlinear phase.[23] However, as shown in Fig. 5, the zonal flow shear correlation with residual stress ($C[\Pi^R_{r\phi}, \omega_{ZF}] \approx -0.5$ during $250 < t \times v_{ti}/L_{Te} < 500$) is significantly weaker than that with the intensity gradient, so zonal flow shear appears not to be responsible for the $\Pi^R_{r\phi}$ orientation change at weak $\hat{s}$.

The effect of $\hat{s}$ and q on $\Pi^R_{r\phi}$ orientation change can be examined by parametric scans of $\hat{s}(r_c)$ and $q(r_c)$, respectively. In the first set of parametric scan, three q profiles are used and the corresponding equilibria are generated. As shown in the left panel of Fig. 6, the three q profiles have the same $q(r_c)$ but $\hat{s}(r_c) = 0.2$, 0.4, and 0.6, respectively. It is found that the $\Pi^R_{r\phi}$ profiles have the opposite orientations between the $\hat{s}(r_c) = 0.2$ case and the $\hat{s}(r_c) = 0.4$ and 0.6 cases, as shown in the right panel of Fig. 6. Furthermore, we also examine the dependence of residual stress profile structure on q. As shown in the left panel of Fig. 7, the three profiles have different q values, i.e., $q_{(r_c)} = 0.94$, 1.50, and 2.08, respectively, but the same $\hat{s}$, i.e., $\hat{s}(r_c) = 0.4$. It is found that the residual stress profiles have the same orientation although q changes significantly, as shown in the right panel of Fig. 7. These two sets of parametric scans as shown in Figs. 6 and 7 demonstrate that $\hat{s}$ is responsible for the intrinsic torque reversal, while a change in q has no significant effect.

It has been shown previously that turbulence self-generated zonal flow shear can induce $k_\parallel$ symmetry breaking.[23] A sensitivity study is also carried out to assess the effect of zonal flow shear on $\Pi^R_{r\phi}$ orientation change at weak $\hat{s}$. In GTS nonlinear simulations, zonal flow can be filtered out. The effect of zonal flow shear on breaking the radially elongated eddies and reducing the turbulence level has been observed by comparing the turbulence structure and evolution with and without zonal flow. The effect of zonal field induced flow shear on $\Pi^R_{r\phi}$ is also examined. The residual stress profiles with zonal field switched on and off for weak $\hat{s}$ are compared in Fig. 8. The orientation of the $\Pi^R_{r\phi}$ profiles for both cases remains changed compared to that for normal $\hat{s}$ case in Fig. 2(c). This demonstrates that the $\Pi^R_{r\phi}$ reversal at weak $\hat{s}$ is not due to zonal flow shear effect. This is consistent with the results of correlation analysis presented in Fig. 5.

In addition to the effect of the zonal flow, the effect of equilibrium radial electric field E_{r0} (Ref. 31) is also examined. When turning on and off E_{r0}, the observation of $\Pi^R_{r\phi}$ profile reversal from normal to weak $\hat{s}$ remains unchanged. All these studies indicate that $\hat{s}$ is a crucial parameter in determining the intrinsic torque direction and that the zonal and equilibrium E_r flow shear play a weak role in affecting the intrinsic torque reversal at weak $\hat{s}$. It is found that the correlation between intensity gradient and residual stress has the opposite sign at weak $\hat{s}$ compared to that at normal $\hat{s}$. The correlation and sensitivity studies indicate a new

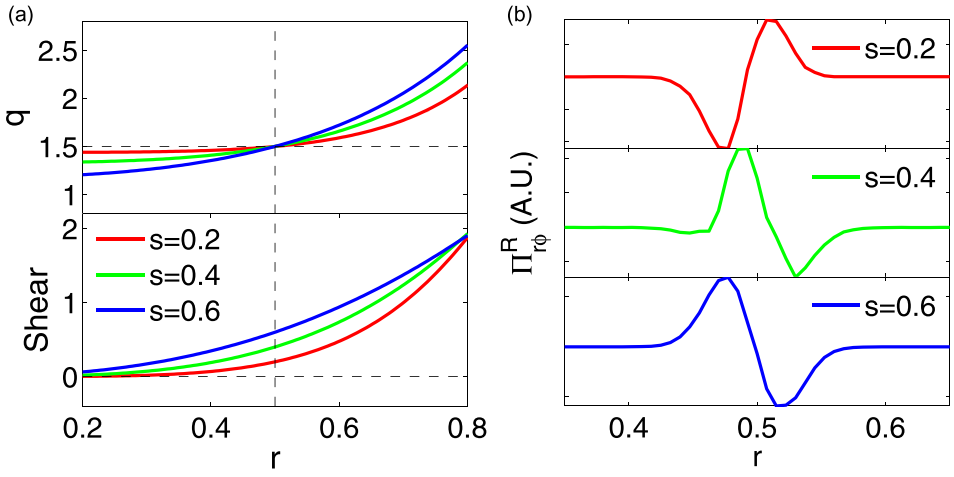

FIG. 6. q and $\hat{s}$ profiles (left); residual stress profiles (right). Different q profiles have the same q value at $r = r_c$, i.e., $q(r_c) = 1.5$, but different $\hat{s}(r_c)$ values, i.e., $\hat{s}(r_c) = 0.2$, 0.4, and 0.6. Residual stress profile changes its orientation for $\hat{s}(r_c) = 2$ compared to that with $\hat{s}(r_c) = 0.4$ and 0.6.

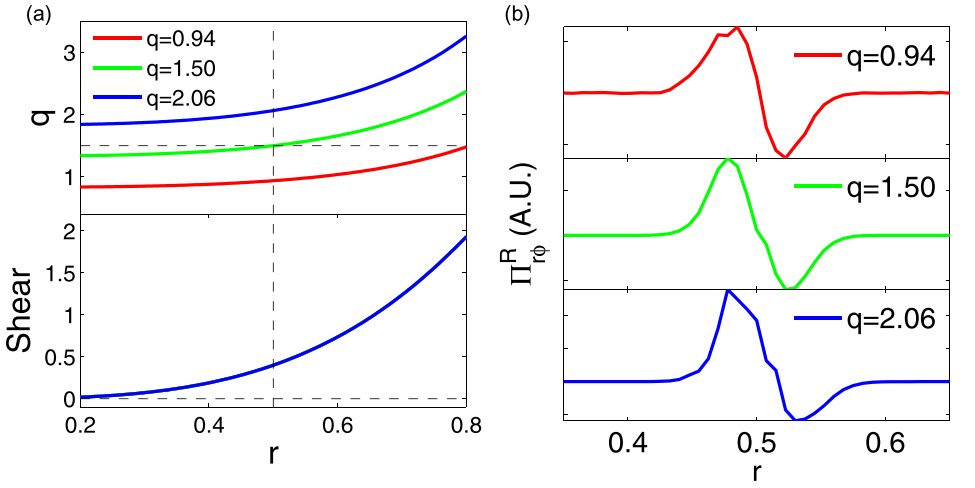

FIG. 7. q and $\hat{s}$ profiles (left); residual stress profiles (right). Different q profiles have different q values at $r = r_c$, i.e., $q(r_c) = 0.94$, 1.50, and 2.06, but the same $\hat{s}(r_c)$, i.e., $\hat{s}(r_c) = 0.4$. Residual stress has the same orientation for the three cases.

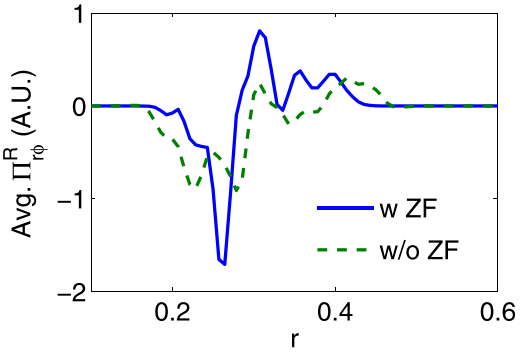

FIG. 8. Residual stress with and without zonal flows for $\hat{s}(r_c) \sim 0.1$. Both cases have the opposite orientation of $\Pi^R_{r\phi}$ compared to that for normal $\hat{s}$ case.

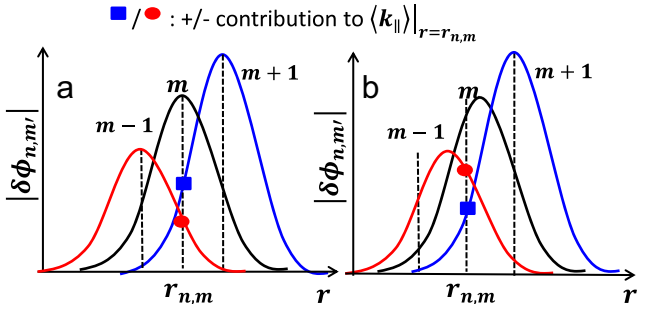

FIG. 9. Cartoons of radial structure of poloidal harmonics for normal (a) and weak (b) shear. For normal $\hat{s}$ (a), $\delta\phi_{m+1}$ contributes more than $\delta\phi_{m-1}$ to $\langle k_\parallel |\delta\phi|^2 \rangle$ at r_m (broken line with markers) and thus $\langle k_\parallel |\delta\phi|^2 \rangle < 0$. For weak $\hat{s}$ case (b), $\delta\phi_{m-1}(r)$ shifts towards the (n, m) mode strongly and sets the sign of $\langle k_\parallel |\delta\phi|^2 \rangle$ although its amplitude is lower than that of $\delta\phi_{m+1}(r)$, yielding $\langle k_\parallel |\delta\phi|^2 \rangle > 0$.

symmetry breaking mechanism at weak $\hat{s}$, which is distinct from the previous ones.[21,31] The underlying physics will be identified in Sec. IV.

IV. INTERPRETATION OF THE INTRINSIC TORQUE REVERSAL BASED ON MODE STRUCTURE ANALYSIS AND RESIDUAL STRESS ESTIMATE

In this section, the underlying physics of the intrinsic torque reversal is identified based on mode structure analyses. To understand the role of $\hat{s}$ in the intrinsic torque reversal, we analyze the radial structure of the poloidal harmonics (radial eigenfunction) $\delta\phi_m(r)$ to demonstrate $\delta\phi_m(r)$'s unusually enhanced radial shift and the consequent $\langle k_\parallel |\delta\phi|^2 \rangle$ reversal at weak $\hat{s}$. Figure 9 shows cartoons of $\delta\phi_m(r)$ for normal (a) and weak $\hat{s}$ (b) cases, based on simulation results. From the analysis in Sec. II, $\langle k_\parallel |\delta\phi|^2 \rangle$ appears strongly correlated with the residual stress and thus we focus on $\langle k_\parallel |\delta\phi|^2 \rangle$. For simplicity, we choose a single n mode and calculate $\langle k_\parallel |\delta\phi|^2 \rangle$ at $r_{n,m}$, the mode rational surface of the harmonic (n, m), where by definition $k_\parallel|_{r_{n,m}} \propto nq - m = 0$. For normal $\hat{s}$, in the presence of intensity gradient, the poloidal harmonics with $m' > m$ (blue line) contribute more to $\langle k_\parallel |\delta\phi| \rangle$ at $r_{n,m}$ than do those with $m' < m$ (red line), and thus $\langle k_\parallel |\delta\phi|^2 \rangle = \sum_{m'} (nq - m')|\delta\phi_{m'}|^2/qR < 0$.[21] However, at weak $\hat{s}$, as shown in Fig. 9(b), the simulations show that the harmonic $m - 1$ shifts towards the harmonic (n, m) so strongly that $\langle k_\parallel |\delta\phi|^2 \rangle$ is set mainly by the modes with lower amplitude, yielding $\langle k_\parallel |\delta\phi|^2 \rangle$ reversal as compared to that in Fig. 9(a). This kind of radial shift was noticed in early studies of ballooning instabilities[32] and is also observed in our global gyrokinetic simulation. The radial shift of the poloidal harmonics at weak $\hat{s}$ is different than that due to equilibrium E_r or zonal E_r shear flow, as verified by the foregoing correlation and sensitivity studies, and is responsible for the residual stress reversal appearing at weak $\hat{s}$.

An analytical interpretation can be obtained from the quasilinear estimate of residual stress and its dependence on $\hat{s}$. The residual stress is estimated as[21]

$$\langle \delta v_r \delta v_\parallel \rangle = -\frac{e}{B_\phi m_i} Re \left\langle \frac{|\gamma_{\mathbf{k}}|}{|\omega_{\mathbf{k}}|^2} \frac{nq}{r} k_\parallel |\delta\phi|^2 \right\rangle. \quad (1)$$

For simplicity, we focus on a single n mode but all its m harmonics, thus $\langle \delta v_r \delta v_\parallel \rangle \propto \langle k_\parallel |\delta\phi|^2 \rangle$. We calculate $\langle k_\parallel |\delta\phi|^2 \rangle$ by referring to the ITG/CTEM eigen equation. By applying 2D mixed complex-WKB-full-wave analysis,[33] the perturbed electric potential is decomposed as $\delta\Phi(r, \hat{\theta}, \zeta, t) = \exp\{-in\zeta + inq\hat{\theta} - i\omega t\} \sum \delta\bar{\phi}(r, \hat{\theta} + 2p\pi) \exp\{2\pi inpq\}$ where $\delta\bar{\phi}(r, \hat{\theta})$ represents the radial envelop $A(r)$ and the parallel mode structure $\delta\hat{\phi}$, i.e., $\delta\bar{\phi}(r, \hat{\theta}) = A(r)\delta\hat{\phi}(r, \hat{\theta})$. The radial envelop can be written in the Eikonal form $A(r) = \exp\{i \int dr n q' \hat{\theta}_k\}$ and the complex wave vector $\hat{\theta}_k \equiv \hat{\theta}_{k,R} + i\hat{\theta}_{k,I}$

describes the radial phase and amplitude variation of the envelop. In the fluid-ion limit,[34,35] the eigen equation yields

$$\left\{\frac{\omega_{ti}^2}{\omega^2}\frac{\partial^2}{\partial\hat{\theta}^2}+\frac{(1+\delta^{NA})/\tau+\omega_{*i}/\omega}{1-\omega_{*pi}/\omega}+Q\right\}\delta\hat{\phi}=0,$$
$$Q=(k_\theta\rho_i)^2\left[1+\hat{s}^2(\hat{\theta}-\hat{\theta}_k)^2\right]-\frac{\omega_D}{\omega}\kappa_c, \quad (2)$$

where $\omega_{ti}=v_i/qR$, $\omega_{*i}=-k_\theta\rho_i v_i/L_n$, $\omega_D=-2k_\theta\rho_i v_i/R$, $\rho_i=v_{ti}/\Omega_{ci}$ is the ion Larmor radius, $v_{ti}=\sqrt{T_i/m_i}$, $\omega_{*pi}=(1+\eta_i)\omega_{*i}$, $\eta_i=d\ln T_i/d\ln n_i$, $L_n=-(d\ln n/dr)^{-1}$, δ^{NA} is the trapped electron non-adiabatic response, and the potential Q consists of the ion FLR term $(k_\theta\rho_i)^2$ and the ion magnetic drift term $\kappa_c=\cos\hat{\theta}+\hat{s}(\hat{\theta}-\hat{\theta}_k)\sin\hat{\theta}$. To calculate $\hat{s}_{crit}$ and demonstrate the effects of magnetic drift and FLR terms, a parametric scan of $\hat{s}$ is performed based on Eq. (2). Other parameters correspond to those of the GTS simulations. The value of n, for the CTEM case, is chosen according to $k_\theta\rho_i=1$. The normalized variable $\langle qR_0k_\parallel\rangle\equiv\sum_m(nq-m)|\delta\phi_m|^2/\sum_m|\delta\phi_m|^2$ is calculated. As shown in the upper panel of Fig. 10, the black line is $\langle qR_0k_\parallel\rangle$ obtained by solving Eq. (2), and as the baseline, it shows that when $\hat{s}$ decreases from normal to weak, $\langle qR_0k_\parallel\rangle$ crosses $\langle qR_0k_\parallel\rangle=0$ at $\hat{s}_{crit}=0.38$. If we choose $\kappa_c=0$, $\langle qR_0k_\parallel\rangle$ always remains positive and is close to a saturation value, indicating that the negative value of $\langle qR_0k_\parallel\rangle$ at weak $\hat{s}$ results from the magnetic drift term. The other curves have FLR and κ_c terms artificially suppressed or amplified by multiplying different factors α_κ and α_{FLR}. They show that increasing κ_c and decreasing ion FLR effect have a similar impact on increasing $\hat{s}_{crit}$ as compared to the baseline. This trend can be demonstrated by the parametric scan with respect to $\alpha_\kappa/\alpha_{FLR}$, as shown in the lower panel of Fig. 10. The blue broken line with square markers gives the critical value $\hat{s}_{crit}$ with $\alpha_\kappa=1$ and varying α_{FLR}. The magenta triangles indicate $\hat{s}_{crit}$ with $\alpha_{FLR}=1$ and varying α_κ. These two curves overlap quite well and show that the increase of $\alpha_\kappa/\alpha_{FLR}$ leads to the increase of $\hat{s}_{crit}$. This demonstrates that the competition between the FLR and κ_c terms determines the value of $\hat{s}_{crit}$, at which $\langle qRk_\parallel\rangle=0$. This competition is reminiscent of the transition between the toroidal branch and the slab branch of the drift wave, related to $\hat{s}$.[35] However, the previous work focused on the eigenfrequency and not on the asymmetry of the parallel mode structure. The novelty of the analysis in this work is the consideration of the synergy of the toroidal coupling and intensity gradient effects. On one hand, the magnetic drift term $\kappa_c=\cos\hat{\theta}+\hat{s}(\hat{\theta}-\hat{\theta}_k)\sin\hat{\theta}$ introduces toroidal coupling which brings in modulations on the otherwise anti-well potential Q.[35] On the other hand, the radial intensity gradient in $\hat{\theta}_k$ introduces symmetry breaking in κ_c. The synergy of these two effects leads to the radial eigenfunction shift and reversal of $\langle qR_0k_\parallel\rangle$ at weak $\hat{s}$. Notice that the intensity gradient also appears in the FLR term and leads to symmetry breaking and residual stress. This corresponds to the previous proposed symmetry breaking mechanism[21] and is not responsible for the $\langle qR_0k_\parallel\rangle$ reversal at weak $\hat{s}$.

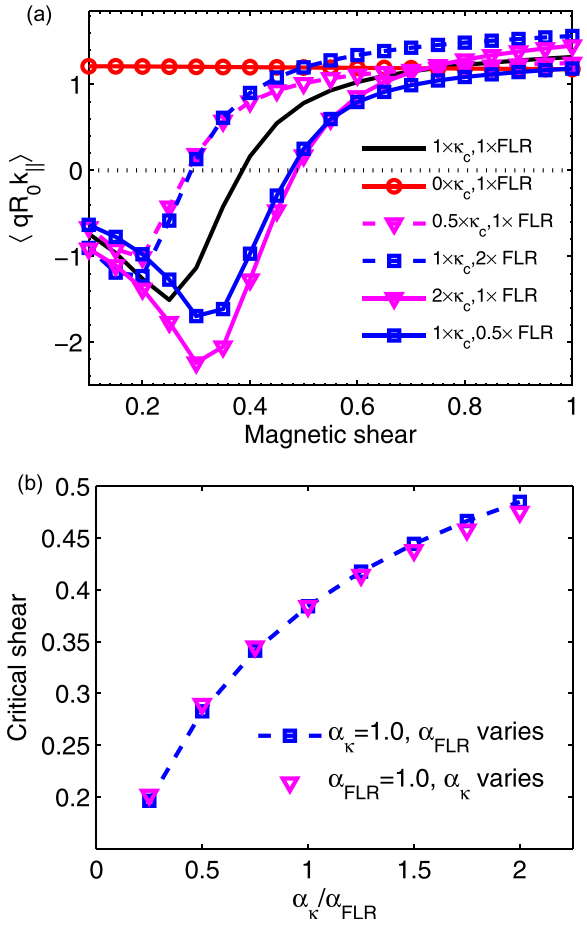

FIG. 10. $\langle qR_0k_\parallel\rangle$ with different amplification factors of magnetic drift (κ_c) and ion FLR effect (upper). The black line is $\langle qR_0k_\parallel\rangle$ obtained from Eq. (2) for CTEM branch, while the other lines are that with different amplification factors α_{FLR} or α_κ for FLR or κ_c terms. Critical magnetic shear versus $\alpha_\kappa/\alpha_{FLR}$ (lower).

It can be shown that the radial eigenfunction shift occurs when this new symmetry breaking due to the synergy of the toroidal coupling and the intensity gradient effects at weak $\hat{s}$ is present. The radial eigenfunction shift, i.e., poloidal harmonic $\delta\phi_m(r)$'s radial shift, can be obtained as $\Delta r_m=(-1/nq')(2|\sigma|^2\hat{\theta}_{k,I}/\sigma_R-qR_0\langle k_\parallel\rangle)$, based on the connection formula,[33] where $\sigma=-i(\omega_{ti}/\omega)\sqrt{b-[(\hat{s}-1/2)C+i\hat{s}\hat{\theta}_{k,I}S/2]\omega_D/\omega}$, $b=(k_\theta\rho_i\hat{s})^2$, $S=\sin\hat{\theta}_{k,R}$, $C=\cos\hat{\theta}_{k,R}$. In Eq. (2), at normal to large $\hat{s}$, FLR effects ($\propto\hat{s}^2$) dominate over the magnetic drift term κ_c ($\propto\hat{s}$). An analytical solution can be obtained as $\langle k_\parallel\rangle|_{\hat{s}\to\infty}=(2/qR_0)(|\sigma|^2\hat{\theta}_{k,I}/\sigma_R)$. This shows that $\Delta r_m|_{\hat{s}\to\infty}=0$, i.e., $\delta\phi_m(r)$ peaks at its rational mode surface as $\hat{s}\to\infty$. When $\hat{s}$ decreases, the magnetic drift effects become important, inducing significant radial shift, which causes $\langle k_\parallel\rangle$ reversal. It should be noted that Eq. (2) does not include zonal flow or equilibrium flow, thus the radial shift in the weak $\hat{s}$ regime discussed here is indeed a new mechanism for $k_\parallel$ symmetry breaking, distinct from previous results which relied on the $E\times B$ shear symmetry breaking mechanism.[21,23]

V. RELEVANCE TO EXPERIMENTAL RESULTS AND CONCLUSIONS

Our finding of critical magnetic shear for the intrinsic torque reversal gives an interpretation of the Alcator C-Mod

TABLE II. The parameters of C-Mod high I_p and low I_p discharges (shot numbers: 1110128020 and 1110128015). n_0, T_{i0} T_{e0}, and B_0 are on-axis values while elongation and triangularity coefficients characterize the outer boundary flux surface for solving the magnetic equilibria.

	n_0 (10^{14}/cm^3)	T_{i0} (keV)	T_{e0} (keV)	B_0 (T)	Elongation	Triangularity
High I_p	1.01	1.32	2.98	5.3	1.31	0.27
Low I_p	1.06	0.90	1.76	5.2	1.43	0.26

experimental results. The high and low plasma current (I_p) discharges in Ref. 15 produce core $\hat{s}$ values which appear in the $\hat{s}_{crit}^{CTEM} < \hat{s} < \hat{s}_{crit}^{ITG}$ and $\hat{s} < \hat{s}_{crit}^{CTEM}$ regimes of Table I, respectively. In addition, the high and low I_p discharges are CTEM and ITG dominated, respectively, according to GTS simulations with realistic plasma profiles and thus, are located in regime II and VI in Table I. The prediction of torque reversal from the high to low I_p discharges based on Table I agrees with the experimental results. Based on the realistic temperature and density profiles, as well as the equilibria, characterized by the parameters in Table II, the residual stress calculated from the GTS simulation shown in Fig. 11 has the opposite orientations for the normal and weak core magnetic shear cases, and the torque direction at the inner (small r) region agrees with that of the experimental observations. Moreover, the experimentally observed critical magnetic shear, $\hat{s}_{crit}^{exp} = 0.2 \sim 0.3$,[15] is consistent with our analysis, i.e., $\hat{s}_{crit}^{CTEM} \approx 0.3$. The direction of ΔV_ϕ or the intrinsic torque, as well as the critical magnetic shear for reversal, is recovered in the simulation. It should be noted that in Secs. I–IV, we adopted higher temperatures and a lower toroidal magnetic field compared to C-Mod parameters, which reduces the normalized minor radius from $a/\rho_i > 300$ (C-Mod) to $a/\rho_i \approx 160$ (Sec. I) and makes the parametric scans affordable. In addition, in order to identify the

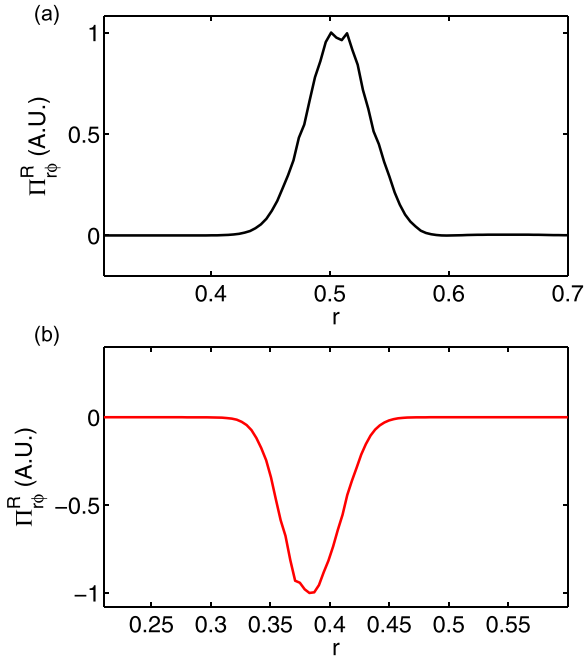

FIG. 11. Residual stress during linear stage for normal core $\hat{s}$ (upper) and weak core $\hat{s}$ (bottom) cases.

underlying physics of intrinsic torque reversal, we focus on specific turbulence (CTEM or ITG) by specifying analytical temperature and density profiles as mentioned in Sec. I, which are different than the experimental ones in this section. However, the simulation based on the realistic C-Mod profiles in this section demonstrates the relevance of our proposed new mechanism to the experimental observations. Detailed comparisons between the simulation and experimental results rely on better controlled parametric scan data (e.g., changing $\hat{s}$ without ITG-TEM transition) in experiments as well as more in-depth simulation, and will be done in future work.

In conclusion, a new mechanism for the intrinsic torque reversal linked to weak magnetic shear $\hat{s}$ is identified based on our simulations and analyses. The main results of this paper are as follows:

(1) Intrinsic torque τ_I reversal for weak $\hat{s}$ is found in simulation; τ_I reverses when $\hat{s} < \hat{s}_{crit}^{CTEM} \approx 0.3$ for CTEM and when $\hat{s} < \hat{s}_{crit}^{ITG} \approx 1.3$ for ITG, without requiring negative $\hat{s}$. For both ITG and CTEM turbulence, the intrinsic torque is counter-current directed when $\hat{s} > \hat{s}_{crit}^{ITG}$ and changes to co-current directed when $\hat{s} < \hat{s}_{crit}^{CTEM}$. In the intermediate $\hat{s}$ regime, ITG and CTEM induce co- and counter-current directed intrinsic torque, respectively.
(2) Correlation and sensitivity studies support that the symmetry breaking mechanism of residual stress due to intensity gradient is dominant at weak $\hat{s}$, while zonal flow shear or equilibrium flow shear plays minor role in the intrinsic torque reversal. The parametric scans of $\hat{s}$ and q, respectively, show that $\hat{s}$ but not q is more relevant to the intrinsic torque reversal at weak $\hat{s}$.
(3) Analysis identifies that the τ_I reversal is due to the dominance of a new symmetry breaking mechanism at weak $\hat{s}$, in particular, the radial eigenfunction shift due to the synergy of toroidal coupling and intensity gradient. This new mechanism is peculiar to toroidal geometry and is not just the continuation of the traditional intensity gradient symmetry breaking mechanism to weak $\hat{s}$.[21]
(4) Based on realistic parameters of C-Mod LHCD experiments, simulation demonstrates that the intrinsic torque changes from counter- to co-current direction as core $\hat{s}$ changes from normal to weak and ITG changes to CTEM, which is consistent with experimental observations. The critical value of $\hat{s}$ for reversal calculated from the simulations, i.e., $\hat{s}_{crit} \approx 0.3$, is also consistent with that observed in the experiments.

Our finding of a new mechanism for intrinsic torque reversal could be important for interpreting experimental results on other tokamak devices and for understanding the total toroidal rotation profile formation as well as its consequences. The keys points can be described as follows:

(1) Based on our findings, it is suggested that the database of the rotation experiments might be better classified and that the intrinsic torque direction might be better predicted according to the magnetic shear, mode type, and other parameters. The rotation reversal of Ohmic discharges has been observed on various tokamak devices

such as TCV,[36] ASDEX Upgrade,[37] and C-Mod,[12] where the critical density is more relevant, while the effects of magnetic shear have been essentially ignored until the recent LHCD rotation experiments.[15] Realizing the new mechanism of intrinsic torque linked to weak $\hat{s}$ might help classify the results of all these experiments in a multiple-parametric space including density, magnetic shear, etc., and to guide future experiments.

(2) Given that the intrinsic torque at weak or negative magnetic shear may play an important role in ITB formation,[16] an important question to ask is how and if possible transport changes at weak $\hat{s}$ occur. To this end, we state that complex interactions of external and intrinsic torque are possible. The Optimal Shear (OS) experiments on JET demonstrated that increased $E \times B$ flow shear and decreased $\hat{s}$ result in ITB formation.[18,19] Although the $E \times B$ flow shear is mainly due to toroidal rotation induced by neutral beam (NB) for co or counter-current injection in those cases,[18] understanding the contribution of intrinsic torque becomes important when net NB momentum is negligible or comparable to external injected momentum, as done in "balanced" cases on JET[18,20] and "cancellation" experiments on DIII-D,[9] or when the toroidal rotation cannot be efficiently driven by NBI on large-size devices such as ITER or DEMO. In these cases, the effects of the new mechanism linked to weak $\hat{s}$ could be significant on ITB formation, which is relevant to the ITER hybrid scenario, where $\hat{s}$ is weak in the core.[38]

An extension of this work could be the comparison of this new mechanism of intrinsic torque with momentum diffusion and pinch in various parametric regimes. In addition, it might be important to consider turbulent acceleration,[39,40] polarization drift,[41] turbulence spreading,[42] and their behavior at weak magnetic shear. Understanding the direction and characteristic dependence of the intrinsic torque due to the new mechanism in this work is crucial to understanding whether the torque adds to or cancels other mechanism, e.g., E_r shear mechanism, turbulent acceleration, as well as external torque, and how the plasma thus accesses de-stiffened and ITB states.

ACKNOWLEDGMENTS

This work was supported by CER, DOE Grant for CMTFO DE-FG02-OER54871, and U.S. DOE-PPPL Contract No. DE-AC02-09CH11466. The support from L. Zakharov on equilibrium files and from J. Chen on computation is acknowledged. Simulations were performed on Edison at the National Energy Research Scientific Computing Center (NERSC). Z.L. appreciates the hospitality of PPPL during his visit. Z.L. appreciates the discussion with F. Zonca on 2D mode structure analysis.

[1]G. Rüdiger, *Differential Rotation and Stellar Convection: Sun and Solar-Type Stars* (Gordon and Breach, New York, 1989).
[2]D. W. Hughes, R. Rosner, and N. Weiss, *The Solar Tachocline* (Cambridge University Press, Cambridge, 2007).
[3]M. P. Baldwin, P. B. Rhines, H.-P. Huang, and M. E. McIntyre, Science **315**, 467 (2007).
[4]U. Frisch, *Turbulence: The Legacy of A. N. Kolmogorov* (Cambridge University Press, Cambridge, 1995).
[5]H. K. Moffatt, *Magnetic Field Generation in Electrically Conducting Fluids* (Cambridge University Press, Cambridge, 1978).
[6]K. Ida, Y. Miura, T. Matsuda, K. Itoh, S. Hidekuma, S.-I. Itoh, and JFT-2M Group, Phys. Rev. Lett. **74**, 1990 (1995).
[7]J. E. Rice, W. D. Lee, E. S. Marmar, N. P. Basse, P. T. Bonoli, M. J. Greenwald, A. E. Hubbard, J. W. Hughes, I. H. Hutchinson, A. Ince-Cushman *et al.*, Phys. Plasmas **11**, 2427 (2004).
[8]P. Diamond, Y. Kosuga, Ö. D. Gürcan, C. McDevitt, T. Hahm, N. Fedorczak, J. Rice, W. Wang, S. Ku, J. Kwon *et al.*, Nucl. Fusion **53**, 104019 (2013).
[9]W. M. Solomon, K. H. Burrell, J. S. deGrassie, R. Budny, R. J. Groebner, J. E. Kinsey, G. J. Kramer, T. C. Luce, M. A. Makowski, D. Mikkelsen *et al.*, Plasma Phys. Controlled Fusion **49**, B313 (2007).
[10]A. Bondeson and D. J. Ward, Phys. Rev. Lett. **72**, 2709 (1994).
[11]A. Bortolon, B. P. Duval, A. Pochelon, and A. Scarabosio, Phys. Rev. Lett. **97**, 235003 (2006).
[12]J. E. Rice, I. Cziegler, P. H. Diamond, B. P. Duval, Y. A. Podpaly, M. L. Reinke, P. C. Ennever, M. J. Greenwald, J. W. Hughes, Y. Ma *et al.*, Phys. Rev. Lett. **107**, 265001 (2011).
[13]A. Ince-Cushman, J. E. Rice, M. Reinke, M. Greenwald, G. Wallace, R. Parker, C. Fiore, J. W. Hughes, P. Bonoli, S. Shiraiwa *et al.*, Phys. Rev. Lett. **102**, 035002 (2009).
[14]Y. Shi, G. Xu, F. Wang, M. Wang, J. Fu, Y. Li, W. Zhang, W. Zhang, J. Chang, B. Lv *et al.*, Phys. Rev. Lett. **106**, 235001 (2011).
[15]J. E. Rice, Y. A. Podpaly, M. L. Reinke, R. Mumgaard, S. D. Scott, S. Shiraiwa, G. M. Wallace, B. Chouli, C. Fenzi-Bonizec, M. F. F. Nave *et al.*, Phys. Rev. Lett. **111**, 125003 (2013).
[16]C. D. Challis, Y. F. Baranov, G. D. Conway, C. Gormezano, C. W. Gowers, N. C. Hawkes, T. C. Hender, E. Joffrin, J. Mailloux, D. Mazon *et al.*, Plasma Phys. Controlled Fusion **43**, 861 (2001).
[17]J. Connor, T. Fukuda, X. Garbet, C. Gormezano, V. Mukhovatov, M. Wakatani, the ITB Database Group, the ITPA Topical Group on Transport, and Internal Barrier Physics, Nucl. Fusion **44**, R1 (2004).
[18]T. Tala, J. Heikkinen, V. Parail, Y. F. Baranov, and S. Karttunen, Plasma Phys. Controlled Fusion **43**, 507 (2001).
[19]P. Mantica, C. Angioni, C. Challis, G. Colyer, L. Frassinetti, N. Hawkes, T. Johnson, M. Tsalas, J. Weiland, B. Baiocchi *et al.*, Phys. Rev. Lett. **107**, 135004 (2011).
[20]H. Shirai, M. Kikuchi, T. Takizuka, T. Fujita, Y. Koide, Y. Sakamoto, O. Naito, T. Hatae, A. Isayama, Y. Kamada *et al.*, Plasma Phys. Controlled Fusion **42**, A109 (2000).
[21]Ö. D. Gürcan, P. H. Diamond, P. Hennequin, C. J. McDevitt, X. Garbet, and C. Bourdelle, Phys. Plasmas **17**, 112309 (2010).
[22]J. M. Kwon, S. Yi, T. Rhee, P. H. Diamond, K. Miki, T. S. Hahm, J. Y. Kim, Ö. D. Gürcan, and C. J. McDevitt, Nucl. Fusion **52**, 013004 (2012).
[23]W. X. Wang, T. S. Hahm, S. Ethier, G. Rewoldt, W. W. Lee, W. M. Tang, S. M. Kaye, and P. H. Diamond, Phys. Rev. Lett. **102**, 035005 (2009).
[24]W. X. Wang, P. H. Diamond, T. S. Hahm, S. Ethier, G. Rewoldt, and W. M. Tang, Phys. Plasmas **17**, 072511 (2010).
[25]W. X. Wang, T. S. Hahm, S. Ethier, L. E. Zakharov, and P. H. Diamond, Phys. Rev. Lett. **106**, 085001 (2011).
[26]L. Zakharov and A. Pletzer, Phys. Plasmas **6**, 4693 (1999).
[27]X. Q. Xu and M. N. Rosenbluth, Phys. Fluids **3**, 627 (1991).
[28]F. Hinton and R. Hazeltine, Rev. Mod. Phys. **48**, 239 (1976).
[29]A. E. White, N. T. Howard, M. Greenwald, M. L. Reinke, C. Sung, S. Baek, M. Barnes, J. Candy, A. Dominguez, D. Ernst *et al.*, Phys. Plasmas **20**, 056106 (2013).
[30]T.-H. Watanabe, H. Sugama, and S. Ferrando-Margalet, Phys. Rev. Lett. **100**, 195002 (2008).
[31]Ö. D. Gürcan, P. H. Diamond, T. S. Hahm, and R. Singh, Phys. Plasmas **14**, 042306 (2007).
[32]R. L. Dewar, J. Manickam, R. C. Grimm, and M. S. Chance, Nucl. Fusion **21**, 493 (1981).
[33]Z. X. Lu, F. Zonca, and A. Cardinali, Phys. Plasmas **19**, 042104 (2012).
[34]W. M. Tang, Nucl. Fusion **18**, 1089 (1978).
[35]L. Chen and C. Z. Cheng, Phys. Fluids **23**, 2242 (1980).
[36]B. Duval, A. Bortolon, A. Karpushov, R. Pitts, A. Pochelon, A. Scarabosio, and T. Team, Plasma Phys. Controlled Fusion **49**, B195 (2007).

[37]C. Angioni, R. McDermott, F. Casson, E. Fable, A. Bottino, R. Dux, R. Fischer, Y. Podoba, T. Pütterich, F. Ryter *et al.*, Phys. Rev. Lett. **107**, 215003 (2011).
[38]A. C. Sips, Plasma Phys. Controlled Fusion **47**, A19 (2005).
[39]X. Garbet, D. Esteve, Y. Sarazin, J. Abiteboul, C. Bourdelle, G. Dif-Pradalier, P. Ghendrih, V. Grandgirard, G. Latu, and A. Smolyakov, Phys. Plasmas **20**, 072502 (2013).
[40]L. Wang and P. H. Diamond, Phys. Rev. Lett. **110**, 265006 (2013).
[41]C. J. McDevitt, P. H. Diamond, O. D. Gürcan, and T. S. Hahm, Phys. Rev. Lett. **103**, 205003 (2009).
[42]V. Naulin, J. Juul Rasmussen, M. Dam, and M. Brøns, in *41st EPS Conference on Plasma Physics, Berlin* (2014).